European Journal of Mechanics / A Solids 116 (2026) 105952

Contents lists available at ScienceDirect

European Journal of Mechanics / A Solids

journal homepage: www.elsevier.com/locate/ejmsol

Full Length Article

3D star-shaped lattice metamaterials exhibiting zero Poisson's ratio

Luke Mizzi *, Alexandre Périer

Department of Sciences and Methods for Engineering, University of Modena and Reggio Emilia, Reggio Emilia, Italy

ARTICLE INFO

Keywords:
Mechanical metamaterials
Zero Poisson's ratio
Honeycomb systems
Mechanical properties
Lattice structures

ABSTRACT

Zero Poisson's ratio metamaterials are a peculiar class of metamaterial systems which undergo no lateral deformation upon uniaxial loading. In this work, we propose a new 3D star-shaped lattice metamaterial structure which is specifically designed to exhibit this property in all three principal directions. This system, which is highly anisotropic, can have a tailorable stiffness which is dependent on the geometry of the structure and may be altered according to design specifications without influencing the Poisson's ratio. An analytical model which may be used to predict the mechanical properties of this system was derived and validated through a wide ranging parametric Finite Element simulation run. In addition, a prototype system was produced using additive manufacturing and tested under compressive loading, with Digital Image Correlation techniques confirming the zero Poisson's ratio of the system, which is retained under relatively high-strain loading. It is envisaged that the large versatility and tuneability of this new metamaterial structure make it ideal for future implementation in applications requiring zero Poisson's ratio properties.

1. Introduction

Mechanical metamaterials are a unique class of materials with properties which are geometry dependent. These include systems with negative, counter-intuitive properties which are not commonly found in nature such as a negative Poisson's ratio (auxetics)(Evans et al., 1991), negative stiffness (Churchill et al., 2016) and negative thermal expansion (Lakes, 2007). These properties make these materials useful for a number of specialised applications in fields such as the biomedical and aerospace industries. An interesting class of mechanical metamaterials is that of systems with a zero Poisson's ratio(Soman et al., 2012). Unlike, conventional positive Poisson's ratio systems which contract laterally upon tensile loading and auxetic materials which do the opposite, these systems remain unchanged in the transverse direction under uniaxial compressive or tensile loading. This property is also highly dependent on the architecture of the metamaterial system and there are various geometries which can give rise to this behaviour. This characteristic is also accompanied by useful secondary properties such as cylindrical curvature, which is extremely desirable for biomedical implants such as stents(Mizzi et al., 2014; Wang et al., 2021) since it ensures a constant cross-sectional thickness and eliminates lateral shape changes and sizing problems (Hoseini et al., 2024).

Initial research on zero Poisson's ratio metamaterials focused on exploiting honeycomb structures, such as mixed mode re-entrant and conventional systems and reversed semi-reentrant hybrid configurations (Grima et al., 2010; Attard and Grima, 2011; Grima and Attard, 2011; Olympio and Gandhi, 2010; Chen and Fu, 2018; Naghavi Zadeh et al., 2020; Huang et al., 2018; Chen et al., 2015)–(Grima et al., 2010; Attard and Grima, 2011; Grima and Attard, 2011; Olympio and Gandhi, 2010; Chen and Fu, 2018; Naghavi Zadeh et al., 2020; Huang et al., 2018; Chen et al., 2015). The main idea was to combine negative Poisson's ratio architectures with positive Poisson's ratio systems and by having the respective mechanisms cancel each other out, obtain zero Poisson's ratio. Other proposals for zero Poisson's ratio architectures involve deformation mechanisms which affect only specific components of geometry which influence the global length of the metamaterial system in the loading direction only, leaving the other unchanged. Apart from these, other forms based on tetrachiral honeycombs(Mizzi et al., 2018; Zhong et al., 2019; Miller et al., 2010)–(Mizzi et al., 2018; Zhong et al., 2019; Miller et al., 2010) (which take advantage of shear-directed deformation modes), star-shaped systems (Ai and Gao, 2018; Gong et al., 2022; Mamoun et al., 2025; Liu et al., 2023), mixed-mode rotating metamaterials (Dudek et al., 2023) and aperiodic tessellations (Clarke et al., 2023) have also been designed. Furthermore, 3D variants of these architectures which exhibit zero Poisson's ratio in multiple planes have also been proposed(Hamzehei et al., 2022; Chen et al., 2021; Yang and Ma, 2020)–(Hamzehei et al., 2022; Chen et al., 2021; Yang and Ma, 2020) along with other works involving new strategies such as

* Corresponding author.
E-mail address: luke.mizzi@unimore.it (L. Mizzi).

https://doi.org/10.1016/j.euromechsol.2025.105952
Received 24 August 2025; Received in revised form 4 November 2025; Accepted 15 November 2025
Available online 19 November 2025
0997-7538/© 2025 The Authors. Published by Elsevier Masson SAS. This is an open access article under the CC BY license (http://creativecommons.org/licenses/by/4.0/).

voxel-based mixed architectures by Sahariah et al. (2023) with a zero Poisson's ratio. This approach which involves combining 3D structures with negative and positive Poisson's ratios to achieve an overall zero Poisson's ratio.

Many of these architectures have been specifically developed to exhibit a tailored mechanical response, namely a zero Poisson's ratio coupled with an accompanying Young's modulus and/or specific programmable shape deformation for one specific loading direction only. Given the fact that in most of these cases, zero Poisson's ratio is typically induced by deformation modes which involve specific components of the geometry deforming only when the system is loaded in a specific direction, tailoring these systems to exhibit desired mechanical properties for uniaxial loading in multiple directions can be a challenge since one must ensure that the deformation mechanism functioning in one direction does not influence the others. In this work, our goal was to develop an anisotropic metamaterial geometry capable of exhibiting a zero Poisson's ratio in multiple on-axis directions while also allowing for large tuneability of Young's modulus in each of the three dimensions through variation of the geometric parameters making up the geometry.

In view of this, we have designed a new 3D metamaterial with a zero Poisson's ratio and the capability of exhibiting different Young's moduli in all three principal directions. This new system, which is formed from a star-shaped architecture, was investigated using a parametric finite element simulation run in order to characterise its mechanical properties. An analytical model capable of predicting the mechanical properties of this system on the basis of its geometric parameters was also developed and validate. Finally, a 3D-printed prototype was designed and fabricated followed by experimental testing under compressive loading conditions. The Poisson's ratio of the system was analysed using Digital Image Correlation (DIC).

2. Concept and design

In this section, the geometry of the 3D star-shaped lattice structure is first characterised in its most generalised form, with ten independent geometric parameters. This is followed by an analytical model which allows the designer to predict its on-axis Poisson's ratios and Young's moduli in terms of these parameters.

2.1. Geometry and dimensions

A schematic of a generic 3D star-shaped lattice structure along with the geometric parameters used to define it is shown in Fig. 1. In Fig. 1a, a single representative volume element (RVE) is shown, while the view of the system from the x-, y- and z-directions are illustrated in Fig. 1b, c and d. As evident from these images, from the on-axis viewpoint, the system has the form of a cross-shaped quadratic star with three axes of mirror symmetry. The full lattice supercells with $3 \times 1 \times 1$, $3 \times 1 \times 3$ and $3 \times 3 \times 3$ RVEs are shown in Fig. 1e, f and g (RVEx × RVEy × RVEz).

The geometry of the system may be defined by the following parameters: l, h, θ and t. The parameter l defines the length of the vertical/horizontal ligaments while h is the length of the inclined ribs. The angle θ determines the inclination of the ligaments with length h and can vary from 0° to 90°. The system is made up entirely of ligaments with a constant cross-section, in this case defined by an in-plane thickness variable, t. In each plane, the parameters l, h and θ may be assigned different values. As shown in Fig. 1, three sets of these independent variables may be defined, with l_1, h_1 and θ_1 denoting the variables along the x-direction, l_2, h_2 and θ_2 along the y-direction and l_3, h_3 and θ_3 in the z-direction.

In the schematic shown in Fig. 1, all l_i, h_i and θ_i variables have the same value, resulting in a cubic RVE. However, if different values are

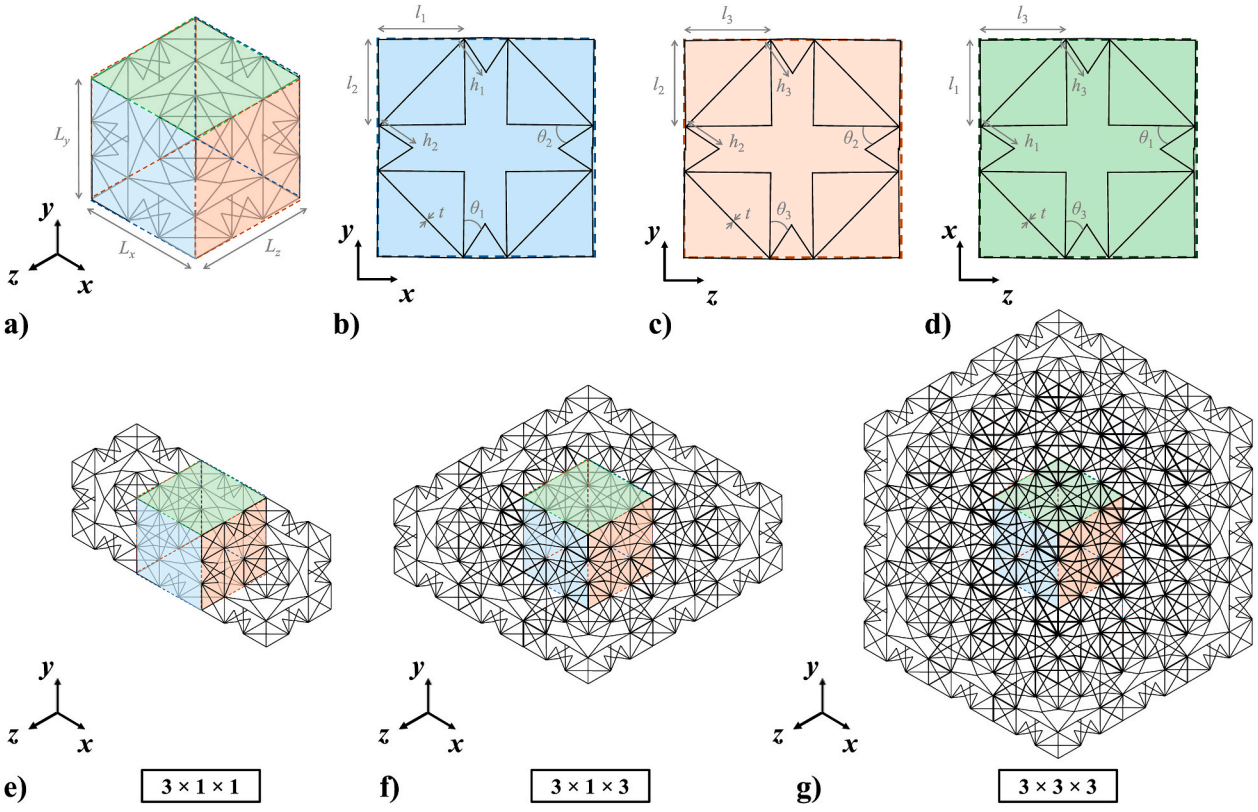


Fig. 1. Schematic of a) an RVE of the proposed star-shaped structure and the view from the b) yx-, c) yz- and d) xz-planes. Images showing the supercells for e) $3 \times 1 \times 1$, f) $3 \times 1 \times 3$ and g) $3 \times 3 \times 3$ RVEs with the central cell marked.

used for these parameters, then a cuboidal RVE is formed. The lengths of the RVE in the three principal directions, L_x, L_y and L_z, may be defined in terms of the independent parameters as follows:

$$\begin{aligned} L_x &= 2(l_1 + h_1 \sin\theta_1) \\ L_y &= 2(l_2 + h_2 \sin\theta_2) \\ L_z &= 2(l_3 + h_3 \sin\theta_3) \end{aligned} \quad \text{Eq. 1}$$

Although the ten geometric parameters are independent, there are some geometric conditions which must be satisfied from combinations of assigned values in order to achieve a realisable system without any overlapping ligaments. These conditions are listed below:

$$\begin{aligned} h_1 \cos\theta_1 &< l_2 + h_2 \sin\theta_2 \\ h_1 \cos\theta_1 &< l_3 + h_3 \sin\theta_3 \end{aligned} \quad \text{Eq. 2}$$

$$\begin{aligned} h_2 \cos\theta_2 &< l_1 + h_1 \sin\theta_1 \\ h_2 \cos\theta_2 &< l_3 + h_3 \sin\theta_3 \end{aligned} \quad \text{Eq. 3}$$

$$\begin{aligned} h_3 \cos\theta_3 &< l_1 + h_1 \sin\theta_1 \\ h_3 \cos\theta_3 &< l_2 + h_2 \sin\theta_2 \end{aligned} \quad \text{Eq. 4}$$

The system was specifically conceived to achieve a zero Poisson's ratio upon uniaxial loading in all three principal on-axis directions. To achieve this, the metamaterial structure was designed on the basis of the principle that in order to maintain a constant lateral width upon the application of a uniaxial load in a direction i, the only components of the system which deform are one set of inclined ligaments, h_i, with the other ligaments remaining undeformed. Since each set of inclined ligaments influences the dimension of the global metastructure in one direction only, this ensures that there is no lateral expansion or contraction, hence guaranteeing a zero Poisson's ratio when the structure is subjected to a uniaxial stresses or strains.

2.2. Analytical model

Based on this design principle and predicted deformation mode, analytical expressions which may be used to predict the in-plane mechanical properties of the star-shaped metamaterials proposed in this work were derived. These expressions consider the linear-elastic deformation of these systems and are based on standard Euler-Bernoulli beam deflection models using the Gibson-Ashby(Gibson et al., 1982) assumptions for deformation of cellular honeycombs. These entail a deformation mechanism which is predominantly characterised by bending/flexure of ligaments with minute contributions from shear and axial deformations and, thus, this model is particularly well-suited for determining the mechanical properties of configurations involving thin, long-ligaments subjected to small-strain loading.

Given the symmetric nature of the metamaterial geometry in question, we can consider the deformation of 1/8th of the RVE in order to characterise this system (see Fig. 2a). This section of the cell can be defined by the following dimensions, denoted as D_x, D_y and D_z:

$$\begin{aligned} D_x &= \frac{L_x}{2} = l_1 + h_1 \sin\theta_1 \\ D_y &= \frac{L_y}{2} = l_2 + h_2 \sin\theta_2 \\ D_z &= \frac{L_z}{2} = l_3 + h_3 \sin\theta_3 \end{aligned} \quad \text{Eq. 5}$$

As shown in Fig. 2b and c, once the system is subjected to a uniaxial load in the x-direction, only one pair of ligaments is expected to deform through bending, while all the other ligaments remain unaffected. This means that all the force generated by the application of stress, σ_x, is absorbed by this ligament pair.

The applied force, F_x, induced by stress can be defined as follows:

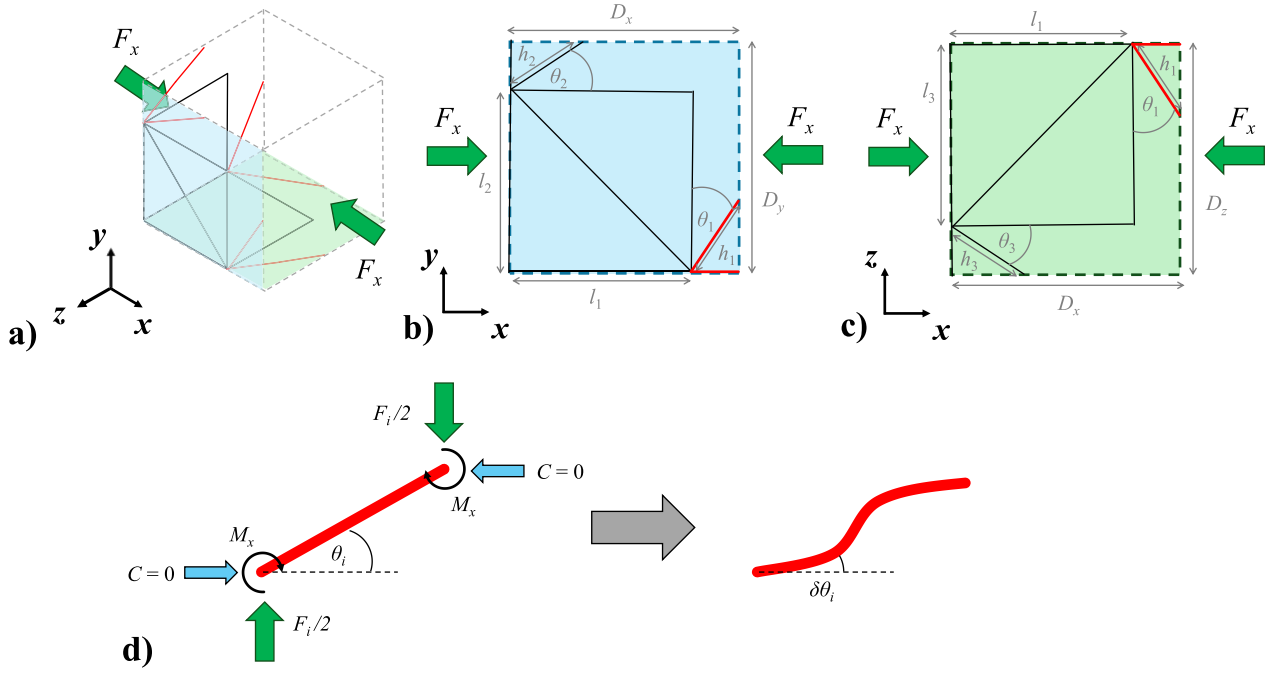


Fig. 2. Image of a) 1/8th of an RVE and the view from the b) yx- and c) xz-planes. The red ligaments indicate the components of the system which undergo deformation upon uniaxial loading in the x-direction. In d) the forces and moments acting on a generic inclined ligament are shown, along with the resultant S-shaped flexural deformation. The reaction force, C, which is perpendicular to the applied load, $F_i/2$ (since there are two ligaments deforming in 1/8th of an RVE), is equal to zero, while the moment, M_x, is calculated according to Eq. (7). (For interpretation of the references to colour in this figure legend, the reader is referred to the Web version of this article.)

$$F_x = \sigma_x D_y D_z \quad \text{Eq. 6}$$

This force generates a moment, M_x, which in turn is defined as:

$$M_x = \frac{F_x}{2}\frac{h_1}{2}\cos\theta_1 \quad \text{Eq. 7}$$

The force is divided by a factor of two since the load is distributed along two ligaments and equilibrium conditions dictate that the reaction force perpendicular to the applied load, C, is equal to zero (see Fig. 2d). From standard beam theory, we can obtain the ligament deflection, δ_x, as:

$$\delta_x = \frac{F_x h_1^3 \cos\theta_1}{24E_s I} = \frac{\sigma_x (l_2 + h_2 \sin\theta_2)(l_3 + h_3 \sin\theta_3) h_1^3 \cos\theta_1}{24E_s I} \quad \text{Eq. 8}$$

Where E_s represents the constituent material isotropic Young's modulus and I the second moment of inertia of the ligament cross-section. The strain in the x-direction, ε_x, generated by this deflection can be defined as follows:

$$\varepsilon_x = \frac{dD_x}{D_x} = \frac{\delta_x \cos\theta_1}{l_1 + h_1 \sin\theta_1} = \frac{\sigma_x (l_2 + h_2 \sin\theta_2)(l_3 + h_3 \sin\theta_3) h_1^3 \cos^2\theta_1}{24E_s I (l_1 + h_1 \sin\theta_1)} \quad \text{Eq. 9}$$

The Young's modulus in the x-direction, E_x, can be found by re-arranging the previous equation as shown below:

$$E_x = \frac{\sigma_x}{\varepsilon_x} = \frac{24E_s I (l_1 + h_1 \sin\theta_1)}{(l_2 + h_2 \sin\theta_2)(l_3 + h_3 \sin\theta_3) h_1^3 \cos^2\theta_1} \quad \text{Eq. 10}$$

Since the deformation of the ligaments shown in Fig. 2b and c, do not result in a global strain in the y- and z-direction for the RVE, the lateral strains ε_y and ε_z are equal to zero. This means that the Poisson's ratios are also equal to zero:

$$\nu_{xy} = -\frac{\varepsilon_y}{\varepsilon_x} = 0 \quad \text{Eq. 11}$$

$$\nu_{xz} = -\frac{\varepsilon_z}{\varepsilon_x} = 0 \quad \text{Eq. 12}$$

Utilising the same reasoning, we can obtain the mechanical properties for loading in the y- and z-directions which result as follows:

$$E_y = \frac{\sigma_y}{\varepsilon_y} = \frac{24E_s I (l_2 + h_2 \sin\theta_2)}{(l_1 + h_1 \sin\theta_1)(l_3 + h_3 \sin\theta_3) h_2^3 \cos^2\theta_2} \quad \text{Eq. 13}$$

$$E_z = \frac{\sigma_z}{\varepsilon_z} = \frac{24E_s I (l_3 + h_3 \sin\theta_3)}{(l_1 + h_1 \sin\theta_1)(l_2 + h_2 \sin\theta_2) h_3^3 \cos^2\theta_3} \quad \text{Eq. 14}$$

$$\nu_{yx} = \nu_{yz} = \nu_{zx} = \nu_{zy} = 0 \quad \text{Eq. 15}$$

Through this analytical model, one may obtain the on-axis Young's moduli and Poisson's ratios of these systems as a function of the basic geometric parameters; the latter of which are all zero provided that the star-shaped lattice framework is employed. In order to investigate further the mechanical properties of this new 3D metamaterial system and validate the predictions of the analytical model, we employed the Finite Element (FE) method to conduct a parametric study, simulating the axial loading behaviour while varying different parameters of the studied shape.

3. Methodology

This section is divided into two parts: a description of the parametric FE simulation run on a large number of configurations and experimental testing of an additively manufactured prototype based on this framework.

3.1. Finite element analysis

A parametric FEM study was carried out on a wide range of configurations to understand the influence of various parameters on the mechanical properties, namely the Poisson's ratios and Young's moduli. The ANSYS Mechanical APDL 2024 software was used to run the simulations and in order to maximise computational efficiency, the structures were moddelled as BEAM elements and simulated as single RVEs under periodic boundary conditions. The systems were meshed using the BEAM189 element (a quadratic three-node 1D beam element with six degrees of freedom (ANSYS24 Multiphysics n)) with a minimum mesh size of 0.2 mm, determined after performing mesh size convergence tests. A square cross-section was used for the beams, with a constant in-plane thickness, t, of 0.1 mm. The constitutive material properties used were an isotropic Poisson's ratio of 0.3 and a Young's modulus of 200 GPa.

The parameters that were modified during this study are: a) the aligned ligament lengths l_1, l_2, and l_3, b) The inclined ligament lengths h_1, h_2, and h_3 and c) the inclination angles θ_1, θ_2, and θ_3. Given the large number of variables at hand, four sets of simulations were carried out. In the first set (Set 1), a cubic RUC was used, with the condition that $h_1 = h_2 = h_3$, $l_1 = l_2 = l_3$ and $\theta_1 = \theta_2 = \theta_3$ kept at all times. The l dimensions were kept constant at 10 mm while the dimensions h and θ varied from 2 mm to 20 mm in steps of 1 mm and 5°–85° in steps of 5° respectively. Following this initial run, further simulations were conducted on systems having cuboidal RVEs in additional three sets. In Set 2, l_2 and l_3 were varied separately from 2 mm to 20 mm in steps of 1 mm, while the other parameters were all kept constant: $l_1 = 10$ mm, $h_1 = h_2 = h_3 = 6$ mm and $\theta_1 = \theta_2 = \theta_3 = 30°$. In Set 3, h_2 and h_3 were varied from 2 mm to 20 mm in steps of 1 mm with all other dimensions fixed at: $h_1 = 6$ mm, $l_1 = l_2 = l_3 = 10$ mm and $\theta_1 = \theta_2 = \theta_3 = 30°$. Finally in Set 4, θ values were varied, with θ_2 and θ_3 changing from 5° to 85° in steps of 5° while $\theta_1 = 30°$, $l_1 = l_2 = l_3 = 10$ mm and $h_1 = h_2 = h_3 = 6$ mm. The full set of simulations are listed in Table 1.

In order to carry out the simulations, the systems were subjected to three separate uniaxial loads in the x-, y- and z-directions under mirror-symmetry based periodic boundary conditions (see Fig. 3). This was possible since the system possesses three planes of mirror-symmetry aligned with the principal global Cartesian directions. To implement these boundary conditions, one face for each of the three principal directions was fixed for one displacement degree of freedom perpendicular to the direction of the surface as shown in Fig. 3. A small compressive displacement was applied on the opposing face according to the loading direction and the remaining two faces were constrained to remain aligned with principal directions using coupling equations. Finally, the rotational degrees of freedom (ROT_x, ROT_y and ROT_z) of all

Table 1
All four sets of simulations carried out listed with the variations in parameters. Note that in Set 1, the variables marked with (*) and (‡) were varied identically with respect to one another.

Set N°	l_1 (mm)	l_2 (mm)	l_3 (mm)	h_1 (mm)	h_2 (mm)	h_3 (mm)	θ_1 (°)	θ_2 (°)	θ_3 (°)
1	10	10	10	2–20 … 1*	2–20 … 1*	2–20 … 1*	5-85 … 5‡	5-85 … 5‡	5-85 … 5‡
2	10	2–20 … 1	2–20 … 1	6	6	6	30	30	30
3	10	10	10	6	2–20 … 1	2–20 … 1	30	30	30
4	10	10	10	6	6	6	30	5-85 … 5	5-85 … 5

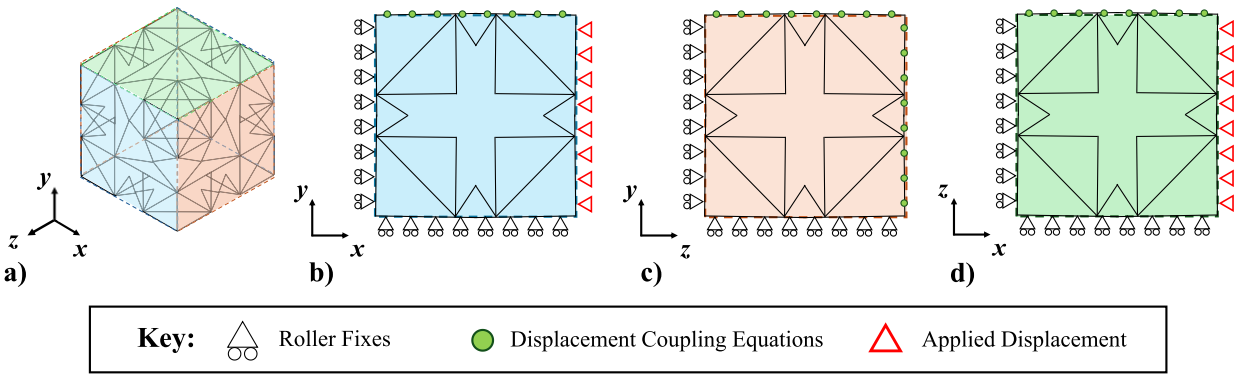


Fig. 3. Images showing how the a) RVE was fixed with viewpoints from the b) *yx*-c) *yz*- and d) *xz*-planes. The constraints were applied on all nodes on the external faces of the RVE. Apart from these constraints, all nodes on opposing faces were individually paired together using coupling equations for the rotational degrees of freedom.

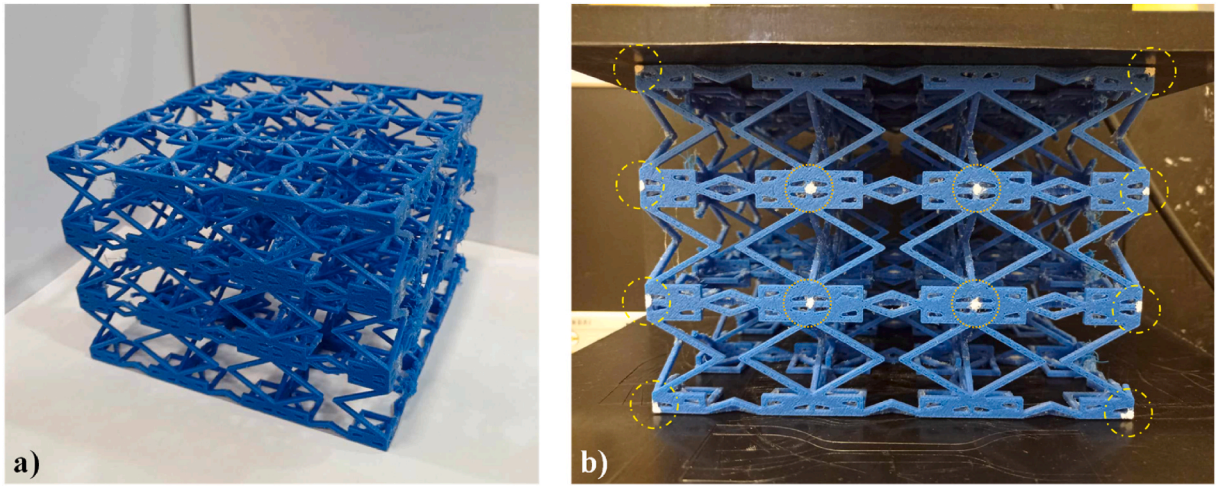


Fig. 4. a) Image of the 3D-printed prototype and b) front-view of the plane in which the Poisson's ratio was measured using DIC, showing the white marker points which were tracked. The points circled in yellow were used to measure the Poisson's ratio from the boundary of the system while the points circled in orange were used to measure the Poisson's ratio of the single central unit cell. (For interpretation of the references to colour in this figure legend, the reader is referred to the Web version of this article.)

external face nodes were paired to the ones on the corresponding opposing face using coupling equations. An example for loading in the *x*-direction is shown in Fig. 3. This methodology is an adaptation of the mirror-symmetry periodic boundary conditions method presented in (Mizzi et al., 2021) and has been validated for use with BEAM elements in (Cavaliere and Mizzi, 2025). The simulations were solved using a linear solver for small strain compressive loading and the three principal Young's moduli, E_x, E_y and E_z, were obtained along with the corresponding six Poisson's ratios, ν_{xy}, ν_{xz}, ν_{yx}, ν_{yz}, ν_{zx} and ν_{zy}.

3.2. Experimental testing

In addition to the simulations, a prototype metamaterial system was designed and produced using additive manufacturing. The system was built using Solidworks CAD software as a 3D 3 × 3 × 3 RVE model and then printed in ABS with 100 % infill using a Stratasys Fortus 250mc FDM printer (see Fig. 4a). The ligaments were built with a square cross-section of thickness, *t*, in an analogous manner to the FE simulations and the corners were filleted with a small radius, *r*. The dimensions of the prototype are listed in Table 2.

Table 2
Geometric parameters of additively manufactured prototype shown in Fig. 4.

l_1	l_2	l_3	h_1	h_2	h_3
15 mm	5 mm	15 mm	10 mm	25 mm	10 mm
θ_1	θ_2	θ_3	*t*	*r*	*RVEs*
70°	30°	70°	2 mm	0.5 mm	3 × 3 × 3

This metamaterial system was specifically designed for optimal loading behaviour in the *y*-direction, with the h_2 ligaments being relatively long in comparison to h_1 and h_3 ligaments, while the angle θ_2 of 30° was also chosen on this basis. The system was therefore subjected to *y*-direction *quasi*-static compressive loading of *ca.* 9 % strain using a Galdabini loading device with two rigid plates placed above and below the system. In order to record the local displacements within the system and measure the Poisson's ratio, 12 points were marked with white paint as shown in Fig. 4b and the entire loading test was recorded by camera. The obtained images were then analysed using a Matlab subroutine for Digital Image Correlation (DIC) point-tracking in order to measure the strain of the system from the tracked points and obtain the Poisson's ratio for a series of images. Two Poisson's ratios were obtained: i) the global Poisson's ratio of entire system, including boundary effects, from the points marked in yellow in Fig. 4b, and ii) the central RVE Poisson's ratio; extracted from the 4 points marked in orange.

4. Results and discussion

The results obtained from the FE simulations, along with the

predictions from the analytical model described in Section 2.2, are presented in Figs. 5–7. It is clearly evident that there is an extremely good match between the analytical predictions and the simulations for both the Poisson's ratios and Young's moduli. In Fig. 5a and b, the results of the Set 1 simulations are presented. As stated previously, this set of simulations comprises of cubic RVEs since $l_1 = l_2 = l_3$, $h_1 = h_2 = h_3$ and $\theta_1 = \theta_2 = \theta_3$ and therefore, all Poisson's ratios and Young's moduli along the principal axes are equal. For this reason, the results are presented in terms of a single Poisson's ratio and Young's modulus. However, it is important to note that this does not entail that the system is isotropic, merely that it exhibits identical mechanical properties at 90° rotational intervals.

The results in Fig. 5a show that almost all configurations in Set 1 exhibit a Poisson's ratio of zero. This Poisson's ratio is the result of the deformation mechanism described in Section 2 and illustrated in the simulation result in Fig. 5c, where only one set of inclined ligaments of length h deforms upon on-axis loading. In the case demonstrated in Fig. 5c, the system is loaded in the x-direction and therefore only the h_1 ligaments undergo flexure upon the application of strain. Analogously, in the case of separate y-direction and z-direction loading, only the h_2 and h_3 ligaments deform respectively. This ensures that no lateral strains occur upon deformation, hence the resultant zero Poisson's ratio. Moreover, the extremely good match between the analytical results and simulation values for the Young's modulus (shown in Fig. 5b), also confirm the presence of this deformation mechanism.

However, as shown in Fig. 5a, there are a few of exceptions for systems with large θ values (>75°) and small h values (<4 mm) which show slightly positive values up to +0.1. They are also characterised by an extremely high stiffness in comparison to the other configurations (see Fig. 5b) due to the very small moment, M_x, generated by the applied force, F_i. These systems are geometrically distinguished by their extremely small inclined ligaments and almost fully-opened aperture angles. This means that the aforementioned deformation mechanism described in the analytical modelling section is not very compliant; in fact, the model is approaching an asymptote at this region. This effect is also observed for regular and re-entrant honeycombs and, at this point, other mechanisms such as direct axial compression of the inclined ligaments come into play rather than pure flexure as demonstrated by Masters and Evans (1996). Nevertheless, as demonstrated clearly in the plots, these structures represent merely a small subset of possible configurations with all the others exhibiting a Poisson's ratio of zero.

This point is plainly emphasised in the Poisson's ratio results obtained from Sets 2, 3 and 4, shown in Fig. 6. These systems are characterised by a cuboidal RVE and are highly anisotropic, yet all exhibit a Poisson's ratio of zero, regardless of the changes in parameters. In the case of Set 2 systems where h_2 and h_3 are varied, the relatively small number of points plotted is due to the realisability conditions stipulated in Eqs. (2)–(4) not being met for several configurations. The uniformity in Poisson's ratios is not, however, mirrored in the Young's moduli plots for the same systems presented in Fig. 7. Here, the large level of

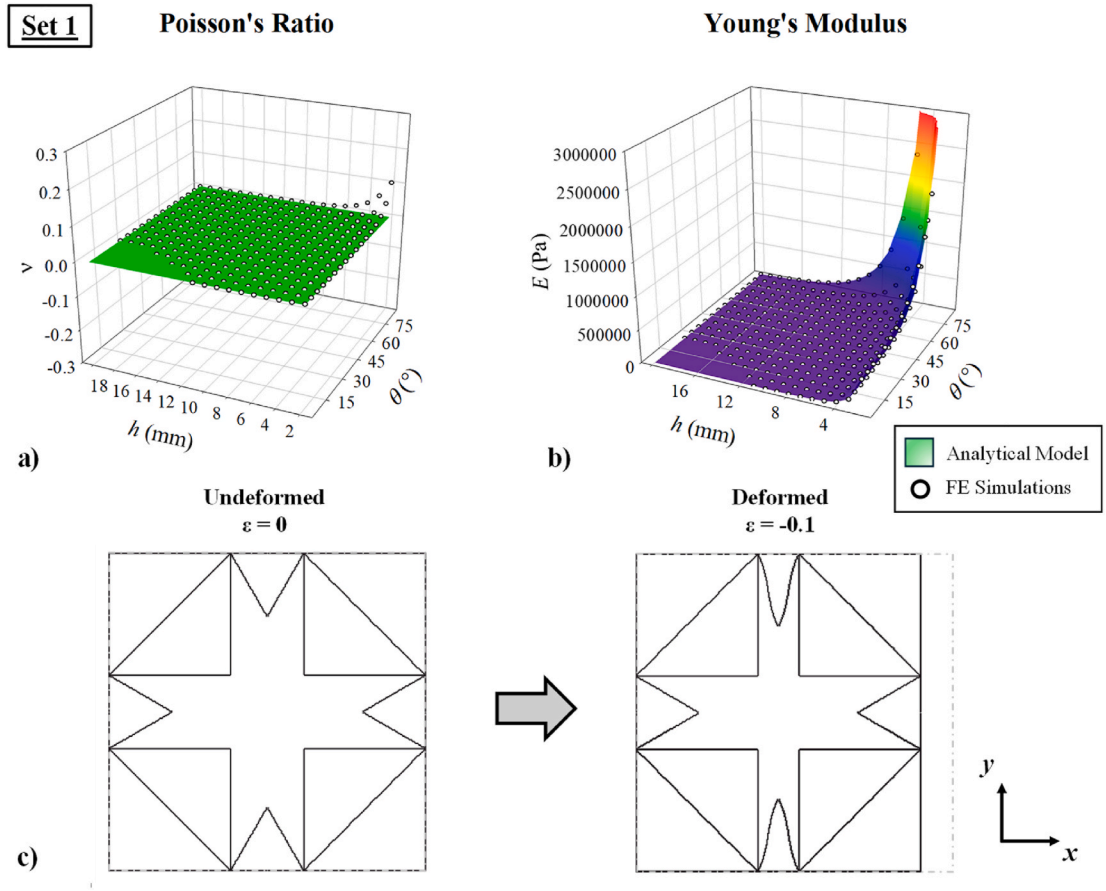


Fig. 5. Plots showing how the a) Poisson's ratio and b) Young's modulus vary with changing h_i and θ_i for the Set 1 simulations and analytical model predictions. Note that, since in this set all the h and θ variables were varied in the same way, the RVE remains cubic and the Poisson's ratios and Young's moduli in the three principal directions are all equal, hence the reason why only two plots are presented. The region without points in both graphs indicates that geometries with that combination of variables are not realisable since they do not satisfy the criteria specified in Eqs. (2)–(4). c) An image of an undeformed and deformed system (with magnified displacement scaling) for compressive loading in the x-direction for the system with $l_1 = l_2 = l_3 = 10$ mm, $h_1 = h_2 = h_3 = 6$ mm and $\theta_1 = \theta_2 = \theta_3 = 30°$.

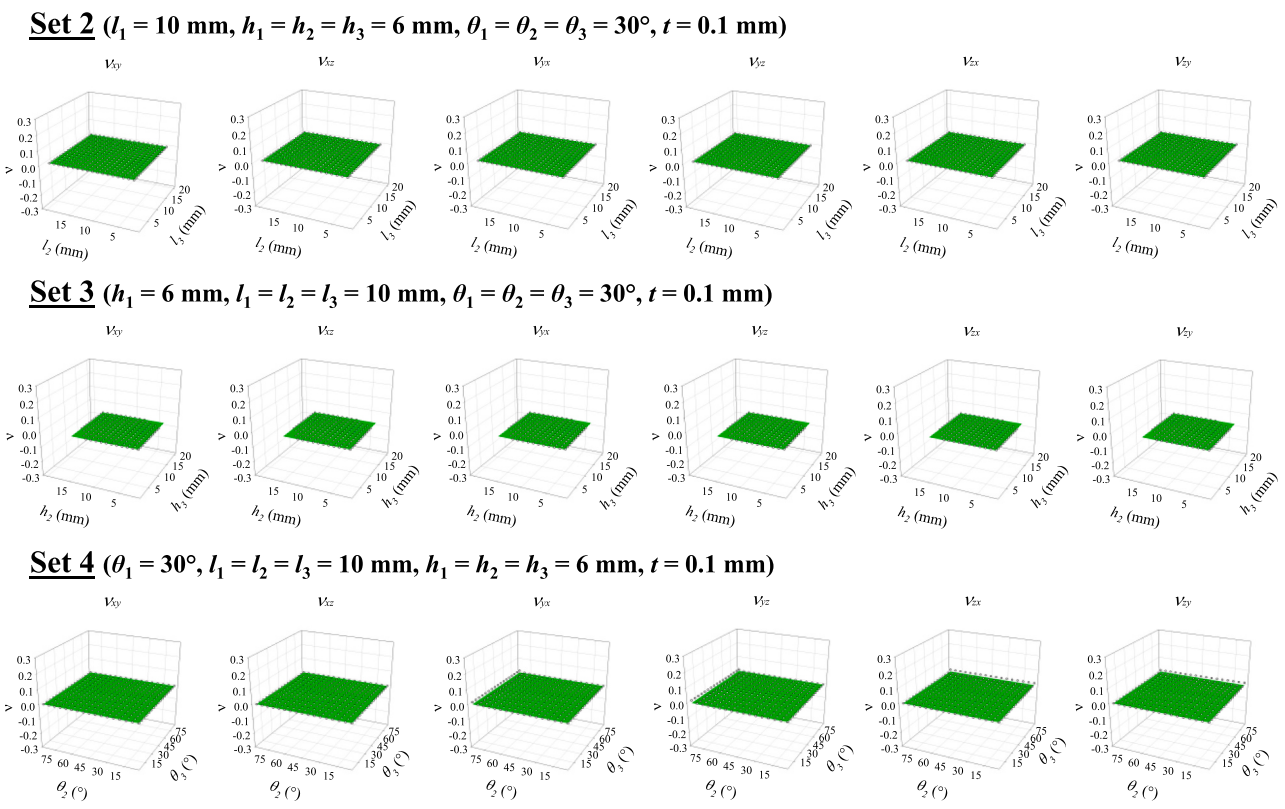


Fig. 6. Plots showing how the on-axis Poisson's ratios vary for Set 2, 3 and 4 structures. The mesh represents the analytical prediction of zero, while the dots are the numerical results obtained from the FE simulations.

anisotropy is clearly demonstrated, with significant variations found in E_x, E_y and E_z for all structures. Starting from Set 2, where parameters l_2 and l_3 are varied, it is evident that the l parameters are ones which have the least significant when it comes to influence on stiffness. This is not surprising, given that these ligaments do not undergo any deformation during loading and, in structural terms, merely define the surface are of the RVE upon which loading is applied. Provided the inverse relationship between l_2 and l_3 with respect to stiffness, E_x, quantified in Eq. (10), it is no surprise to see that for loading in the x-direction, the system shows the highest stiffness when l_2 and l_3 are at their lowest. On the other hand, the opposite is true for E_y and E_z, with large values of l_2 and l_3 resulting in the highest Young's moduli, respectively, in accordance with the predictions from Eqs. (13) and (14).

For Set 3, the variations in h_2 and h_3 show a much greater influence on the Young's modulus. Firstly, as expected, E_x is not very affected by changes in these variables due to the fact that only h_1 ligaments deform upon loading in the x-direction and thus, h_2 and h_3 are only considered for the definition of the surface area of the RVE upon which a load is applied. Conversely, for loading in the y-direction, the length of h_2 is extremely significant, with systems having small ligaments showing the highest stiffness and the same is true for h_3 when loading the z-direction. This is due to the fact that these ligaments are the ones undergoing flexure upon loading in these respective directions, and, thus, in accordance with standard Euler-Bernoulli Beam Theory, the stiffest ligaments for flexural deformations are the shortest.

Finally, for Set 4, where θ_2 and θ_3 are varied, it is shown that these parameters are also extremely influential on the stiffness. For E_x, the same reasoning as above applies, i.e. ligaments with aperture angles θ_2 and θ_3 are not deforming upon loading hence these two parameters only determine the geometry of the RVE and do not have a large influence on stiffness in this direction. For loading in y- and z-directions on the other hand, large θ_2 and θ_3, respectively, yield the highest stiffness. This is due to the fact that the configuration is very close to its fully-opened configuration, i.e. 90°, at which the V-shaped pair of ligaments become a straight line and thus the flexural moment applied by strain becomes almost equal to zero. This leads to an extreme increase in stiffness and, at very large θ angles approaching 90°, most likely results in a change of deformation mechanism and, therefore, a positive Poisson's ratio, as shown in Fig. 5. However, in the configurations presented for Set 3 in Figs. 6 and 7, only a marginal increase in Poisson's ratio is evident and thus these configurations still represent a viable option for high-stiffness zero Poisson's ratio metamaterials.

In order to confirm the zero Poisson's ratio of these systems experimentally, a 3D-printed prototype was produced and tested as detailed in Section 3.3. The images in Fig. 8 show the system before and after deformation, and, along with the plots for the global and central RVE Poisson's ratio, demonstrate quite clearly that the system exhibits a Poisson's ratio of zero which is retained over relatively large strains. This shows that the deformation mechanism which gives rise to this property remains active and unchanged as compressive loading increases. It is also interesting to note that there is also almost no difference between the central RVE and the global system Poisson's ratio. This is anomalous, since in typical auxetic and conventional (positive Poisson's ratio) metamaterials, boundary effects have a significant influence on the deformation behaviour of the structure. However, in this case, the fact that there is no lateral expansion/contraction of the metastructure and that none of the deforming components of the structure are in direct contact with the upper and lower rigid plates, mean that the influence of

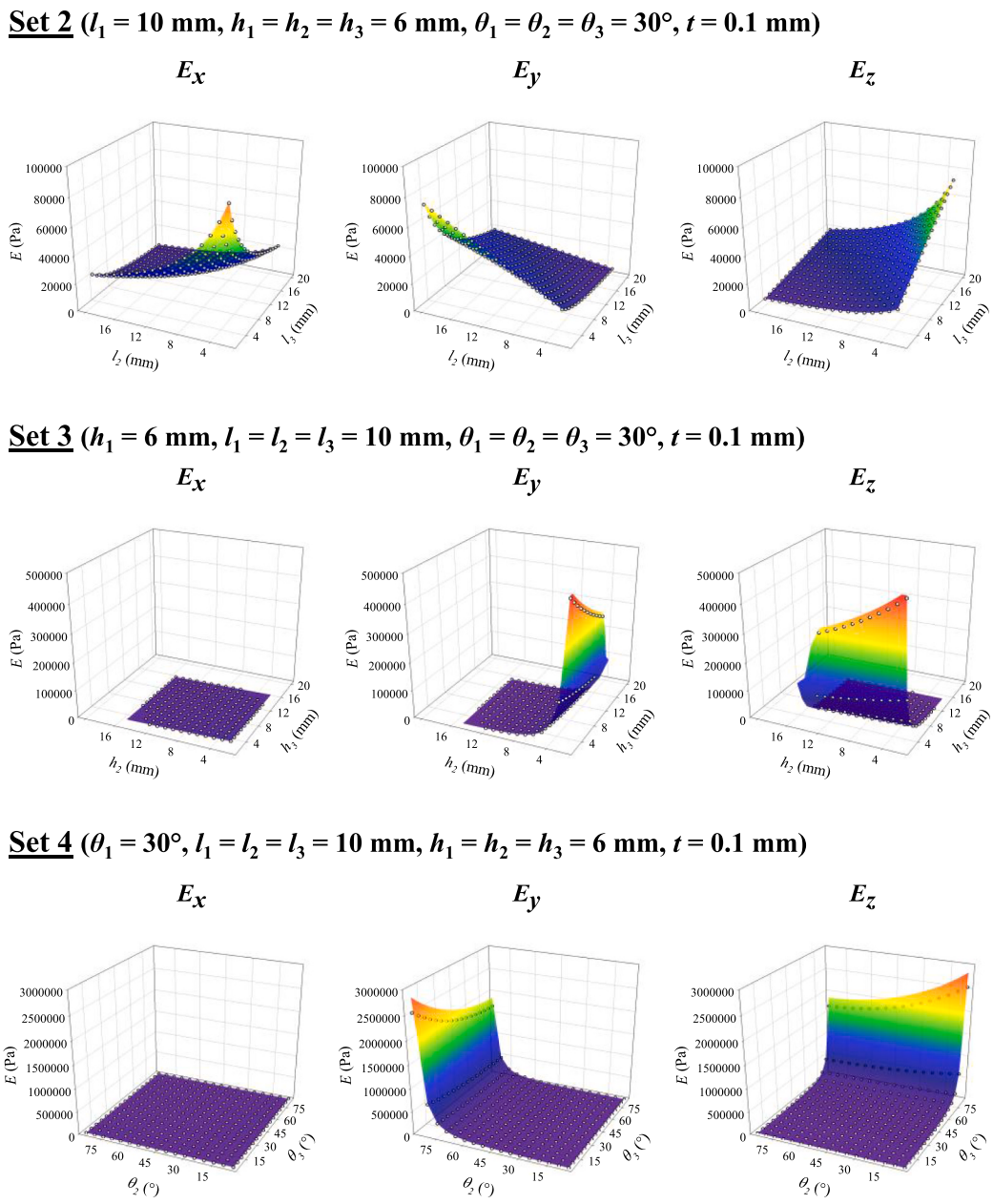


Fig. 7. Plots showing how the on-axis Young's moduli vary for Set 2, 3 and 4 structures. The mesh represents the analytical prediction of zero, while the dots are the numerical results obtained from the FE simulations.

friction on the deformation mechanism is almost negligible and therefore the global system deforms similarly to a periodic RVE.

Before concluding, it is important to highlight the merits of this new star-shaped lattice structure. The main advantage is the zero Poisson's ratio in all three principal directions which remains unchanged regardless of which combination of geometric parameters is chosen. This means that one may tailor the Young's moduli of the structure independently of the Poisson's ratio and use the analytical model described in Section 2.2 to produce a fully-customised anisotropic metamaterial lattice structure according to the desired design specifications. Given that the stiffness in each principal direction is primarily determined by a subset of three variables (with the others having a very small influence), it is also very simple to alter the Young modulus in one specific loading direction without significantly altering the properties in other directions. Moreover, since the structure is entirely ligament-based, it can also qualify as a lightweight structure, and since the volume fraction of the system may be varied as a function of the geometry, one can also design the structure according to the necessary density requirements. Finally, the high strain tolerance and lack of lateral expansion make this metamaterial system ideal for implementation in crash-resistance and dampening applications, although further studies beyond this work are required to analyse the energy absorption and impact properties.

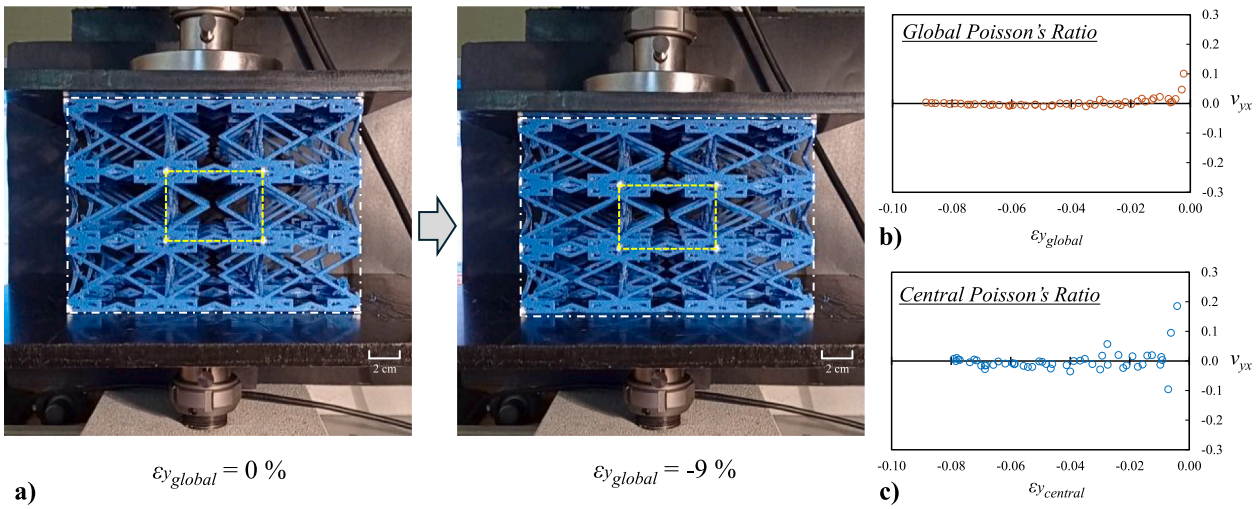


Fig. 8. a) Images showing the prototype before and after loading. The white dashed lines indicate the global dimensions of the system which were used to extract the global engineering Poisson's ratio plotted in b) while the yellow lines show the central RVE from which the central engineering Poisson's ratio in c) was plotted. The increase in noise in plot c) with respect to plot b) is due to the fact that the same images were used for both DIC analysis and in the former the distances between points are significantly smaller than in the latter. (For interpretation of the references to colour in this figure legend, the reader is referred to the Web version of this article.)

5. Conclusion

In this work, a new anisotropic 3D star-shaped lattice metamaterial which exhibits zero Poisson's ratio in all three principal directions is investigated. The stiffness of the system was shown to be tuneable as function of a set of independent geometric variables while the Poisson's ratio remains unchanged. An analytical model which may be used to predict the on-axis mechanical properties of this structure was derived and validated using a wide ranging parametric FE simulation run followed by experimental tests on an additively-manufactured prototype. These findings demonstrate the functionality and effectiveness of this new metamaterial geometry which make it a useful addition to the emergent class of zero Poisson's ratio metamaterials.

CRediT authorship contribution statement

Luke Mizzi: Writing – original draft, Software, Methodology, Investigation, Funding acquisition, Formal analysis, Conceptualization. **Alexandre Périer:** Methodology, Investigation, Formal analysis.

Declaration of competing interest

The authors declare that they have no known competing financial interests or personal relationships that could have appeared to influence the work reported in this paper.

Acknowledgements

This work was supported by the Fondazione Cariplo and Fondazione CDP grant no. 2023-2526 "Support for Young Italian Researchers in ERC Competitions" awarded to Luke Mizzi.

Data availability

Data will be made available on request.

References

Ai, L., Gao, X.L., 2018. An analytical model for star-shaped re-entrant lattice structures with the orthotropic symmetry and negative Poisson's ratios. Int. J. Mech. Sci. 145, 158–170. https://doi.org/10.1016/j.ijmecsci.2018.06.027.
ANSYS24 Multiphysics n.d..
Attard, D., Grima, J.N., 2011. Modelling of hexagonal honeycombs exhibiting zero Poisson's ratio. Phys. Status Solidi B Basic Res. 248, 52–59. https://doi.org/10.1002/pssb.201083980.
Cavaliere, M., Mizzi, L., 2025. Hierarchical honeycomb metamaterials based on monohedral Triangular, square and hexagonal tessellations. Mater. Res. Express.
Chen, Y., Fu, M.H., 2018. Mechanical properties of a novel zero poisson's ratio honeycomb. Adv. Eng. Mater. 20. https://doi.org/10.1002/adem.201700452.
Chen, J., Shen, X., Li, J., 2015. Zero Poisson's ratio flexible skin for potential two-dimensional wing morphing. Aerosp Sci Technol 45, 228–241. https://doi.org/10.1016/j.ast.2015.05.011.
Chen, X., Fu, M.H., Li, W.H., Sheshenin, S.V., 2021. An unusual 3D metamaterial with zero poisson's ratio in partial directions. Adv. Eng. Mater. 23. https://doi.org/10.1002/adem.202001491.
Churchill, C.B., Shahan, D.W., Smith, S.P., Keefe, A.C., McKnight, G.P., 2016. Dynamically variable negative stiffness structures. Sci. Adv. 2.
Clarke, D.J., Carter, F., Jowers, I., Moat, R.J., 2023. An isotropic zero Poisson's ratio metamaterial based on the aperiodic 'hat' monotile. Appl. Mater. Today 35. https://doi.org/10.1016/j.apmt.2023.101959.
Dudek, K.K., Mizzi, L., Iglesias Martínez, J.A., Spaggiari, A., Ulliac, G., Gatt, R., et al., 2023. Micro-scale graded mechanical metamaterials exhibiting versatile Poisson's ratio. Compos. Struct. 319. https://doi.org/10.1016/j.compstruct.2023.117151.
Evans, K.E., Nkansah, M.A., Hutchinson, I.J., Rogers, S.C., 1991. Molecular network design. Nature 353, 124.
Gibson, L.J., Ashby, M.F., Schajer, G.S., Robertson, C.I., 1982. The mechanics of two dimensional cellular materials. Proceedings of the Royal Society A 382, 25–42.
Gong, X., Ren, C., Sun, J., Zhang, P., Du, L., Xie, F., 2022. 3D Zero poisson's Ratio honeycomb structure for morphing wing applications. Biomimetics 7. https://doi.org/10.3390/biomimetics7040198.
Grima, J.N., Attard, D., 2011. Molecular networks with a near zero Poisson's ratio. Phys. Status Solidi B Basic Res. 248, 111–116. https://doi.org/10.1002/pssb.201083979.
Grima, J.N., Oliveri, L., Attard, D., Ellul, B., Gatt, R., Cicala, G., et al., 2010. Hexagonal honeycombs with zero Poisson's ratios and enhanced stiffness. Adv. Eng. Mater. 12, 855–862. https://doi.org/10.1002/adem.201000140.
Hamzehei, R., Serjouei, A., Wu, N., Zolfagharian, A., Bodaghi, M., 2022. 4D metamaterials with zero poisson's ratio, shape recovery, and energy absorption features. Adv. Eng. Mater. 24. https://doi.org/10.1002/adem.202200656.
Hoseini, F., Bellelli, A., Mizzi, L., Pecoraro, F., Spaggiari, A., 2024. Self-expanding Nitinol stents for endovascular peripheral applications: a review. Mater. Today Commun. 41. https://doi.org/10.1016/j.mtcomm.2024.111042.
Huang, J., Liu, W., Tang, A., 2018. Effects of fine-scale features on the elastic properties of zero Poisson's ratio honeycombs. Mater. Sci. Eng., B 236–237, 95–103. https://doi.org/10.1016/j.mseb.2018.11.005.
Lakes, R., 2007. Cellular solids with tunable positive or negative thermal expansion of unbounded magnitude. Appl. Phys. Lett. 90. https://doi.org/10.1063/1.2743951.
Liu, W., Zhang, Y., Guo, Z., Li, D., Zhao, S., Xie, W., 2023. Analyzing in-plane mechanics of a novel honeycomb structure with zero Poisson's ratio. Thin-Walled Struct. 192. https://doi.org/10.1016/j.tws.2023.111134.
Mamoun, O., Ajaj, R., Zweiri, Y., Scarpa, F., 2025. The Quadcomb: a novel zero Poisson's ratio honeycomb structure with 2D compliance for morphing aircraft applications. Mater. Des. 257. https://doi.org/10.1016/j.matdes.2025.114512.
Masters, I.G., Evans, K.E., 1996. Models for the elastic deformation of honeycombs. Compos. Struct. 35, 403–422.

Miller, W., Smith, C.W., Scarpa, F., Evans, K.E., 2010. Flatwise buckling optimization of hexachiral and tetrachiral honeycombs. Compos. Sci. Technol. 70, 1049–1056. https://doi.org/10.1016/j.compscitech.2009.10.022.

Mizzi, L., Attard, D., Casha, A., Grima, J.N., Gatt, R., 2014. On the suitability of hexagonal honeycombs as stent geometries. Phys. Status Solidi B Basic Res. 251, 328–337. https://doi.org/10.1002/pssb.201384255.

Mizzi, L., Mahdi, E.M., Titov, K., Gatt, R., Attard, D., Evans, K.E., et al., 2018. Mechanical metamaterials with star-shaped pores exhibiting negative and zero Poisson's ratio. Mater. Des. 146, 28–37. https://doi.org/10.1016/j.matdes.2018.02.051.

Mizzi, L., Attard, D., Gatt, R., Dudek, K.K., Ellul, B., Grima, J.N., 2021. Implementation of periodic boundary conditions for loading of mechanical metamaterials and other complex geometric microstructures using finite element analysis. Eng. Comput. 37, 1765–1779. https://doi.org/10.1007/s00366-019-00910-1.

Naghavi Zadeh, M., Dayyani, I., Yasaee, M., 2020. Fish Cells, a new zero Poisson's ratio metamaterial—Part I: design and experiment. J. Intell. Mater. Syst. Struct. 31, 1617–1637. https://doi.org/10.1177/1045389X20930079.

Olympio, K.R., Gandhi, F., 2010. Zero poisson's ratio cellular honeycombs for flex skins undergoing one-dimensional morphing. J. Intell. Mater. Syst. Struct. 21, 1737–1753. https://doi.org/10.1177/1045389X09355664.

Sahariah, B.J., Baishya, M.J., Namdeo, A., Khanikar, P., 2023. A novel strategy to design lattice structures with zero Poisson's ratio. Eng. Struct. 288. https://doi.org/10.1016/j.engstruct.2023.116214.

Soman, P., Fozdar, D.Y., Lee, J.W., Phadke, A., Varghese, S., Chen, S., 2012. A three-dimensional polymer scaffolding material exhibiting a zero Poisson's ratio. Soft Matter 8, 4946–4951. https://doi.org/10.1039/c2sm07354d.

Wang, C., Zhang, L., Fang, Y., Sun, W., 2021. Design, characterization, and 3D printing of cardiovascular stents with zero poisson's ratio in longitudinal deformation. Engineering 7, 979–990. https://doi.org/10.1016/j.eng.2020.02.013.

Yang, H., Ma, L., 2020. 1D to 3D multi-stable architected materials with zero Poisson's ratio and controllable thermal expansion. Mater. Des. 188. https://doi.org/10.1016/j.matdes.2019.108430.

Zhong, R., Fu, M., Yin, Q., Xu, O., Hu, L., 2019. Special characteristics of tetrachiral honeycombs under large deformation. Int J Solids Struct 169, 166–176. https://doi.org/10.1016/j.ijsolstr.2019.04.020.